10.21611/qirt.2023.10

Thermographic visualization of non-stationary high speed flow in a channel

by I. Znamenskaya*, M. Muratov*, E. Karnozova*, A. Lutsky**

* *Lomonosov Moscow State University, Leninskie Gory, 1, 119991 Moscow, Russia, muratov583@gmail.com*
** *Keldysh Institute of Applied Mathematics, Miusskaya pl. 4, 125047 Moscow, Russia*

Abstract

This paper explores the possibility of non-invasive heat fluxes visualization and analysis of high speed channel flows using infrared thermographic registration. Panoramic IR imaging was performed as the plane shock wave have passed through the test chamber and diffracted on a rectangular obstacle ($6\times2\times48\,mm$) on the wall in the shock tube channel ($24\times48\,mm$). The evolution of the heat fluxes maps on the test chamber inner walls (IR-transparent windows) are recorded using a high-speed infrared recorder with operating range $1.5-5.1\,\mu m$. The images of thermal fields were compared with shadow imaging and two-dimensional numerical simulation of the non-stationary gas-dynamics flow around after the shock wave diffraction on the ledge.

1. Introduction

The interaction of streamlined surfaces with high-speed gas-dynamic flows has consistently posed a substantial challenge, impacting both fundamental scientific research and practical applications. The emerging heat exchange between the flow and streamlined surfaces of varied geometry leads to significant alterations in the flow structure and parameters of the gaseous medium [1, 2]. The necessity to consider intricate heat and gas dynamic processes has sparked significant interest in employing diverse techniques for flow visualization [3, 4]. This emphasis on visualization methods not only enhances our grasp of fluid dynamics but also plays a crucial role in refining engineering designs and optimizing various applications, ensuring greater efficiency and safety in real-world scenarios. The advancement of digital techniques for optical visualization of rapid processes in liquids and gases has broadened the scope of spatiotemporal parameters available for studying these phenomena. [5, 6]. In this work a relatively new non-intrusive diagnostic method in the field of pulsed gas dynamics - infrared thermography was used. The key advantages of this technique is the possibility of recording the thermal radiation of the object surfaces and its direct conversion into a temperature map [7]. The use of infrared thermography in gas-dynamic problems harnesses the benefits of panoramic non-invasive techniques, capitalizing on their superior spatial resolution, which allows for comprehensive coverage of thermal and gas-dynamic processes, even in scenarios with possible large spatial gradients of measured values [8]. However, despite the significantly higher absolute measurement error, the acquired two-dimensional thermal radiation intensity distributions from surfaces provide fundamentally novel insights into the flow dynamics. Experimental studies of the unsteady heat fluxes dynamics were conducted from the inner quartz walls surfaces of a shock tube based on the technique of high-speed infrared thermography with sub - millisecond time resolution. The studies were accomplished during the propagation of a plane shock wave with Mach numbers $M=2.0-4.5$ inside the channel, its diffraction on a rectangular obstacle located on the floor of the shock channel and evolution of a near-surface co-current flow behind it.

Thermographic and shadowgraph high-speed frame-by-frame visualization of the supersonic and transonic flow in the channel is carried out through the quartz side walls of the working chamber of the shock tube that are transparent in the visible and infrared range.

2. Experimental setup

2.1 Shock tube

The experiments were conducted on a single-diaphragm facility UTRO-3 – a shock tube ($24\times48\,mm$) with high and low pressure chambers separated by a thin polymeric diaphragm (Fig. 1). By choosing the diaphragm thickness and the pressure ratio between the chambers, it was possible to adjust the Mach number of the incident shock wave in the range of $M=2.0-4.5$ at an initial air pressure of $P=100\,Pa$. The incident shock velocity was measured by piezoelectric sensors in the driven section (Fig. 1 A). The formation of plane shock wave was at a distance of about a meter from the diaphragm. The velocity of the co-current flow behind the shock wave front was estimated in the range of $630-920\,m/s$. The Reynolds number of the flow, calculated by the width of the tube channel, was $Re\sim10^5$.

At a distance of $200\,cm$ downstream the diaphragm there was a test chamber with side quartz windows transparent in the infrared range (bandwidth $200-2800\,nm$). A rectangular polymer obstacle ($6\times2\times48\,mm$) with a low thermal conductivity was installed transversely to the oncoming flow (Fig. 1 D). The homogeneous supersonic co-current flow formed behind the shock wave front in the test chamber lasted for up to $500\,\mu s$, until the arrival of the contact surface. The driven and driver gases were air and helium, respectively. The length of high and low pressure chambers is $52\,and\,290\,cm$; dimensions

of side quartz windows - $170 \times 15 \times 24\,mm$. Sensors connected to an oscilloscope (Fig. 1 C) synchronized the thermal imager recording or shadow recording with various stages of the gas-dynamic processes occurring in the test chamber.

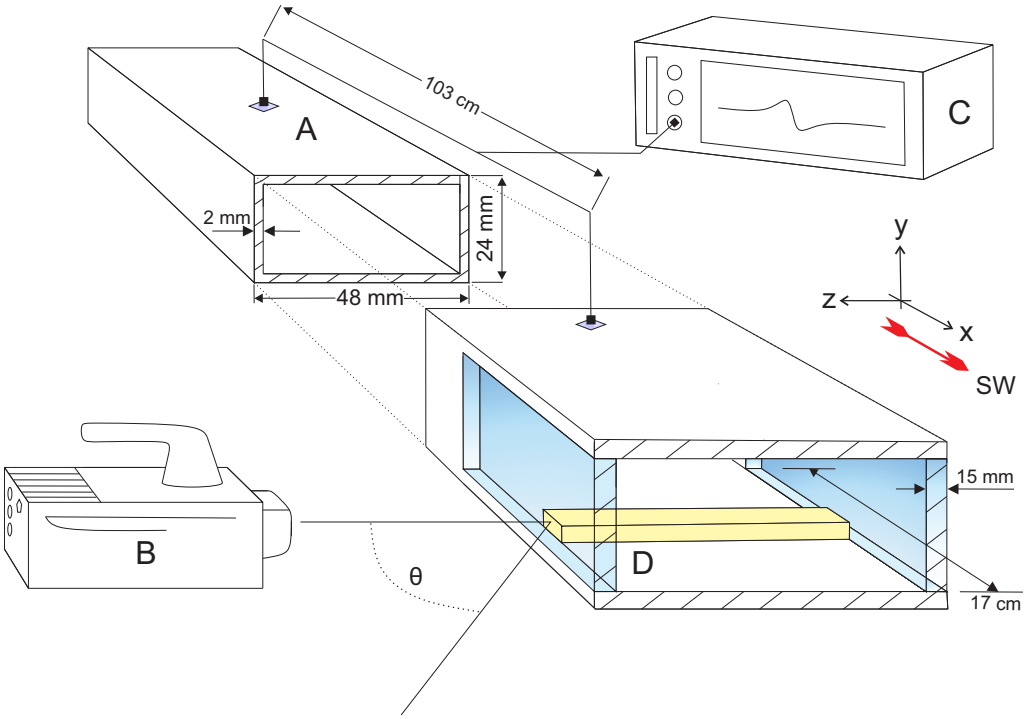

Fig. 1. *Experimental setup scheme*

2.2 Shadow imaging

Shadow shooting of the gas-dynamic flow of the high speed flow was carried out using the laser shadow scheme in parallel beams with a high-speed camera. A shadow scheme with a stationary laser as a light source (wavelength $532\,nm$) was used. The optical beam passed perpendicular to the camera glasses in the area of the stepped obstacle. The optimal shooting speed was $150,000\,frames\ per\ second$ with an exposure of $1\,\mu s$. To improve the quality of shadow images, a script for processing source images with subtraction of the background frame was used.

2.3 Thermographic visualization

A high–speed, cooled, high-resolution photon detector was used as an infrared radiation receiver (Fig. 1 B): Telops Fast M200 (operating range $1.5 - 5.1\,\mu m$).

During the experiments, the infrared recorder was installed at a distance of $25 - 30\,cm$ from the channel wall, while the optical axis was usually directed perpendicular to the main axis of the shock tube (with a possible deviation by some angle to observe regions of interest). The heat fluxes were measured from the windward and leeward sides of the installed obstacle inside the channel as well as from the inner surfaces of the test chamber quartz walls heated by the supersonic and transonic flow behind the shock. Reducing the spatial resolution of the receiver by several times made it possible to record heat fluxes at a frequency up to $2000\,frames/s$. The acquisition time ranged from $200\,\mu s$ up to 1 ms.

It is worth noting that the thermal imager software employed in experiments is configured to the absence of any medium other than the air between the shooting object and the recorder. Otherwise, the equations used to calculate the total radiation flux by the detecting device need to include additional terms related to the presence of an intermediate medium. Thus, the presence of a permeable quartz glass along the camera optical axis prevents accurate quantitative assessments of thermal fields.

3. Results and discussion

Flow with plane shock wave interaction with a rectangular obstacle (ledge) includes the non-stationary processes of diffraction, reflection and streamlining. The resulting quasi-two-dimensional flow around an obstacle consists of a set of

unsteady gas-dynamic structures: a bow shock, an oblique shock, a recirculation zone in the obstacle leeward region, an expanding wave fan (Prandtl–Meyer fan), reattachment shock, etc (Fig. 2). Diffraction of the passing shock wave occurs in $20 - 30\,\mu s$, and then the reflected shock wave slowly moves away from the obstacle towards the flow in times of $200 - 300\,\mu s$, depending on the Mach number of the incident wave.

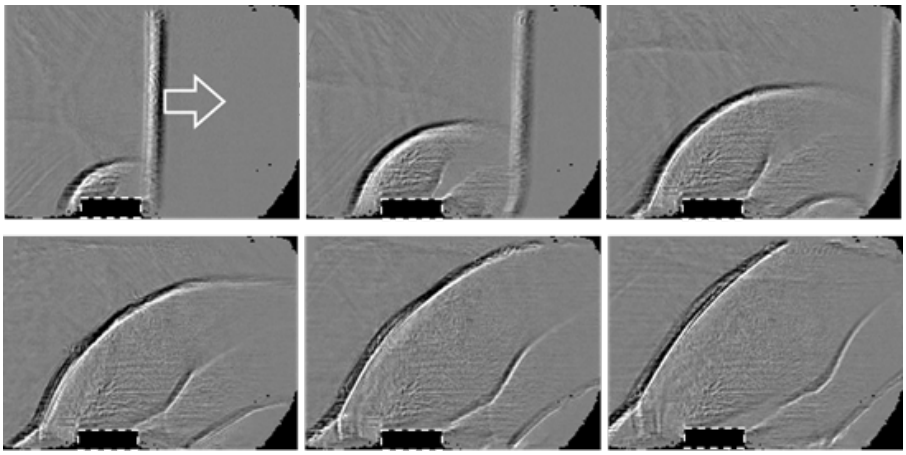

Fig. 2. *Frame-by-frame visualization of shock wave diffraction ($M = 3.1$) made by shadow optical method, $f = 150000\,frame/s$*

3.1 Numerical simulation

Numerical simulation of the considered flow was implemented via the usage of the two-dimensional Navier-Stokes equations. The main task of modeling was to study the movement and the evolution of mainstream splits. More subtle effects, such as the interaction of shock waves with boundary layers on the channel walls and obstacles, were excluded. The algorithm[9] is based on the generalized Godunov scheme with piecewise linear TVD reconstruction of gas-dynamic functions in the cells. Inviscid flows on the cell edges were determined based on exact solutions of the Riemann problem on the edges in the projection to the normal. The velocity and the temperature derivatives required for viscous flows were determined using the Green-Gauss formulas.

The high-velocity flow around the obstacle in the channel is defined by the inhomogeneous density field around the streamlined insert (Fig. 3). The area near the windward wall of the obstacle is characterized by a high degree of density and temperature in the zone of flow deceleration.

$500 - 800\,\mu s$ after the shock wave passage, the flow velocity in the channel decreases due to the arrival of the rarefaction wave. The transonic flow mode is mainly accompanied by the low density area in front of the rectangular ledge and an oblique shock associated with the flow connection. In this mode, the shadow images show an oblique shock shifted to the obstacle trailing edge and a turbulent trail formed by a flow separation behind the obstacle.

The vortex zone of flow separation behind the obstacle is a zone of reduced gas density. Over time, the flow velocity behind the incident shock wave decreases, the flow is turbulized. The results of numerical calculation in the transonic flow mode demonstrate the presence of a rarefaction region where the current lines are curved with the formation of an oblique shock associated with the flow connection.

Comparative analysis of the numerical calculation results of gas-dynamic parameters and experimental frames from high-speed imaging (shadow and infrared) showed a visual similarity of the main structural features of the studied flows.

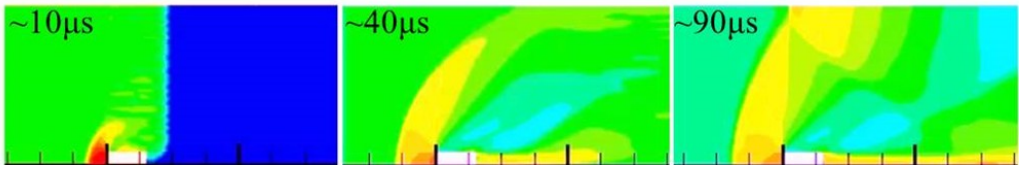

Fig. 3. *Numerical simulation of the flow temperature field: frame-by-frame instantaneous distribution $u = 790 \pm 20\,m/s$ behind the shock wave $M = 3.2$*

3.2 Spatial thermal visualization of heat fluxes

At each stage, the evolution of thermophysical parameters of the flow leads to dynamic temperature and heat fluxes changes in the medium as well as on the streamlined surfaces of the channel: upper and lower walls, obstacle surfaces, side walls (window glasses).

In the boundary layer behind the incident shock wave, the flow velocity rapidly decreases on the surfaces of the channel walls from its maximum value to zero [10]. The velocity gradient of the decelerating gas in the boundary layer leads to the emergence of significant friction forces that dissipate thermal energy to surrounding areas. onsidering this the heat exchange at the interface between the boundary layer and the streamlined surface consists of unsteady thermal conduction, convective heat transfer in the growing turbulent flow and a complex configuration of radiant heat transfer.

As a result, the heat fluxes formed on the inner walls boundary layer penetrates into a rather thin layer of the quartz wall (of the shock tube test section) IR-transparent windows, leaving behind a thermal trace that is visualized by a thermal imager. The successive evolution of the gaseous macroscopic thermodynamic parameters at various stages of shock-wave interaction makes it possible to visualize configurations of a unsteady flow by corresponding changes in heat fluxes between the gas and receptive walls. Their interaction in the boundary layer implements a set of thermal fields on the channel walls according to the proceeding shock diffraction and evolution of the near-surface co-current flow. The resulting integral map of heat fluxes during one shooting frame reflects the distribution of temperature fields in areas of surface flow and on the streamlined surfaces. The corresponding heat map depends on the settings of the thermal imager (frequency, exposure time), camera installation location (observation angle, distance to the survey area), focusing and aligning of the detector as well as the generalized flow state. Adjusting the position and settings of the camera allows to evaluate ongoing gas-dynamic processes with different spatial and temporal resolutions.

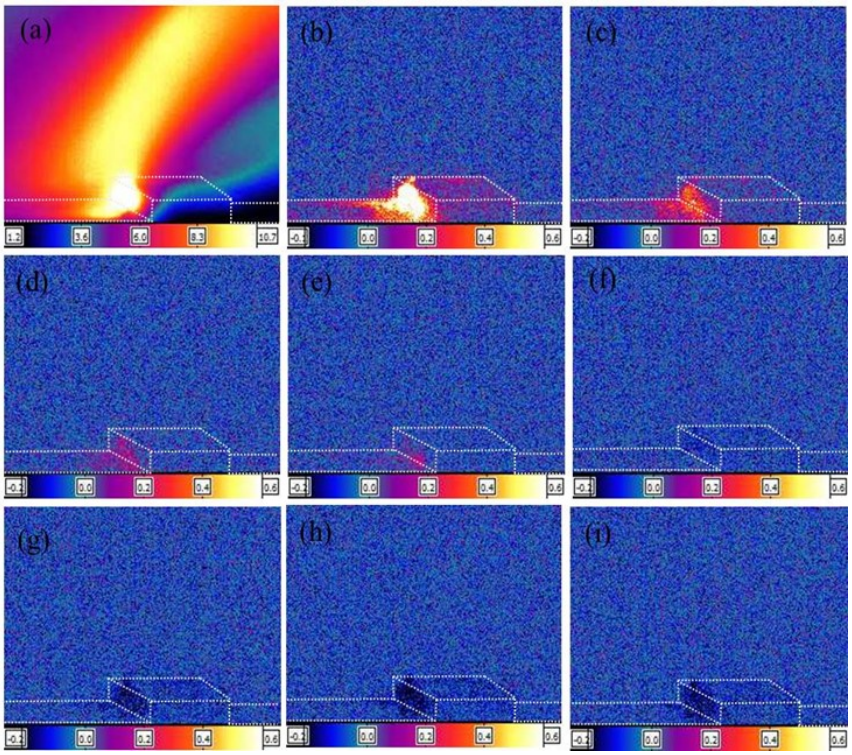

Fig. 4. *The evolution of thermal fields* $M = 4.0$ *after the passage of the shock [windward side;* $\tau_{EXP} = 1000\,\mu s$; $f \approx 600\,Hz$*]: a)* $t = 0\,ms$*; b)* $t = 2\,ms$*; c)* $t = 4\,ms$ *; d)* $t = 6\,ms$ *; e)* $t = 12\,ms$ *; f)* $t = 16\,ms$*; g)* $t = 22\,ms$*; h)* $t = 26\,ms$*; i)* $t = 32\,ms$

Thus, thermographic visualization of the windward edge of an obstacle area obtained at a frequency $f \approx 600\,Hz$ and exposure (acquisition time) $\tau_{EXP} = 1000\,\mu s$ reveal ongoing flow around processes up to $40\,ms$ (Fig. 4). During the first frame ($t = 2\,ms$) (Fig. 4 a) the thermal imager registers the heated (during exposition time) areas of the quartz wall in the near-surface boundary layer corresponding to a reflected outgoing wave forming an area of additional compression and heating in front of the windward side of the ledge. The end of a homogeneous supersonic co-curent flow by an incoming contact surface is identified by an abrupt drop in the averaged radiation level of the survey zone (Fig. 4 b-e). The next few milliseconds, the windward side of the ledge, heated by the decelerating supersonic flow, is visualized, as well as a narrow strip

of the bottom wall of the channel in front of the obstacle. The rarefaction wave significantly reduces the flow temperature. After $t \approx 14\,ms$, a complete decrease in the intensity of thermal radiation from the previously heated obstacle surface area to the background level and below is recorded (Fig. 4 f). Later, the windward side of the obstacle cools down to a $t \approx 20-25\,ms$ (Fig. 4 g–i), followed by a slow recovery to the initial thermal state at $t \approx 40\,ms$.

With increasing shooting frequency (up to $f \approx 2000Hz$) and decreasing exposure time ($\tau_{EXP} = 500\mu s$) the distribution of the obtained thermal fields undergoes significant changes. In this case, the radiation integral flux within one frame acquisition time is reduced by half and at a higher update frequency, flux structures with the largest gradient of measured values are visualized. Given temporal resolution filters low-intensity heat fluxes, highlighting key volumetric flow elements (Fig. 5).

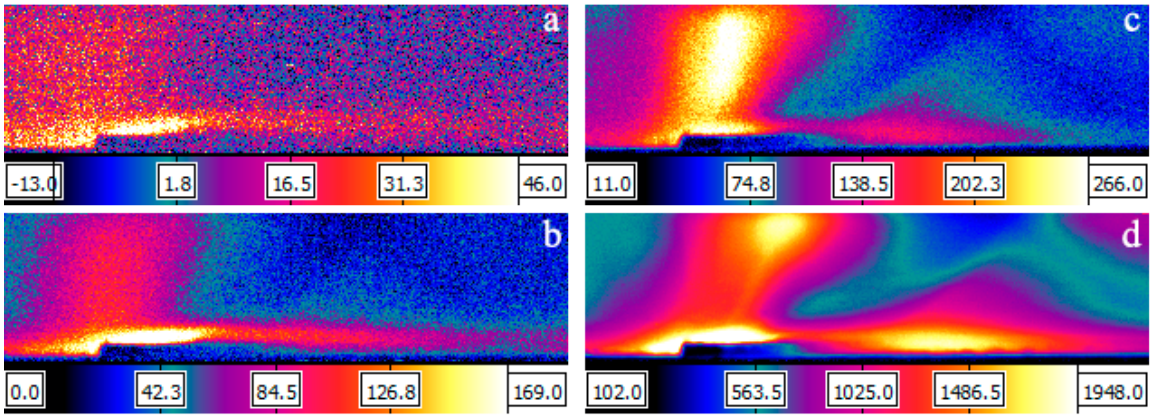

Fig. 5. *Thermographic images (behind the leeward side of the ledge) [$\tau_{EXP} = 500\mu s$; $f \approx 2000Hz$]: a) $M = 2.3$; b) $M = 2.6$; c) $M = 3.0$; d) $M = 4.0$*

The outgoing bow shock (up to $500\,\mu s$) leaves behind an area of elevated temperatures (up to $1000\,K$) in front of the obstacle. As the wave decays, the region of heated gas spreads upstream. Part of the heat from the windward region is carried away by the oncoming high-speed flow. The intensified area in front of the obstacle is also drift downstream by the oncoming co-current flow. Peak radiation is usually detected within the zones of complete flow deceleration, where the hot gas was located for the longest. The heated areas appear to be those in which minimal heat loss is observed during the exposure time. The effect of increased temperature values behind the incident shock wave on the channel walls above the obstacle leads to the formation and integral registration of a heated radiation region in the entire height of the channel. On the leeward side of the insert, recirculation regions and a fan of rarefaction waves are visualized with reduced temperatures and densities (dark blue in Fig. 5).

The velocity of the incident shock wave significantly affects the resulting distribution of thermal fields. For incident shocks of relatively low intensity, the gradient of thermodynamic parameters is insufficient for qualitative visualization of the flow structures. The incoming radiation flux of heated areas during the exposure time resolves areas of increased density and temperature behind the bow shock in front of the ledge (Fig 5a). More intense incident shocks (Fig. 5 b-c) lead to an increase in the relative values and contrast of the recorded thermal images over the entire panoramic heat map. The local radiation maxima of the heated channel wall becomes comparable to the radiation next to the windward side of the obstacle, where the peak radiation value was previously recorded. With an increase in the incident shock wave Mach number, one can note a narrowing of the intensified region in front of the obstacle, as well as an increase in its inclination relative to the channel axis, which indicates a constriction of the bow shock outgoing distance. For Mach numbers above $M \geq 3$ (Fig. 5 d), thermographic images are smoothed, resolving thermal patterns of high and low intensity heat fluxes corresponding to the gas-dynamic structural elements of the flow in the boundary layer.

Since the IR survey was carried out at an angle ($\alpha \approx 25$ relative to the channel) from the leeward wall of the obstacle, the thermal patterns from the internal surfaces of the side walls (front and rear) overlap each other. The integral result of gas-dynamic heating on the front and rear side walls during the exposure time of thermal imaging is schematically presented on Fig 6. Arrows indicate the approximate spreading direction of the flow heated surfaces on the side walls of the channel. At both ends of the obstacle two identical heat fluxes images should be shaped, separated horizontally, in accordance with the two inner surfaces of the heated windows of the test chamber. At working shooting angles in this work, the depicted heating surfaces merged into one continuous gradient surface. However, at extreme shooting angles of a streamlined obstacle, it is possible to obtain separate heat flows from each of the quartz walls of the working chamber of the shock tube.

Consequently, it is shown that thermographic infrared imaging of the thermal fields of the inner surfaces of transparent quartz glasses makes it possible to visualize elements of gas–dynamic structures of unsteady flow adjacent to the windows, hery - after diffraction of a plane shock wave in a channel on a rectangular obstacle.

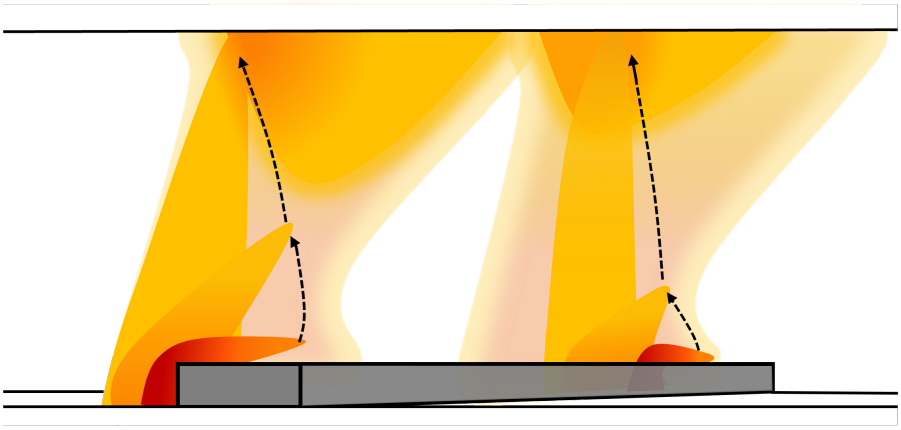

Fig. 6. *Schematic representation of the heat fluxes spreading and overlaying on the channel wall during diffraction of a shock wave on an obstacle*

4. Conclusion

The temporal and temperature resolution of modern thermal imaging detectors make it possible to give a qualitative assessment of transient processes of high-speed gas flows and their realizations for various configurations of streamlined surfaces. Acquired maps of the wall's heat fluxes from the inner channel walls reliably reproduce the complex non-stationary processes inside the channel, considering the heat prorogation due to the conductivity of the walls. Other than that, it is shown that the panoramic IR measurements through the IR- transparent windows make it possible to visualize elements of gas-dynamic structures of unsteady flow. The images of thermographic flow fields were compared with high speed shadow imaging and 2D CFD simulation images at the shock diffraction and reflection of shocks on a rectangular obstacle.

5. Acknowledgments

This work was supported by the Russian Foundation for Basic Research 23-19-0096.

References

[1] Samson Kutateladze and Alexander Leontev. Heat transfer, mass transfer, and friction in turbulent boundary layers. pages 45–56. Hemisphere Publishing Corp., 1990.

[2] Pedro Volpiani, Matteo Bernardini, and Johan Larsson. Effects of a nonadiabatic wall on supersonic shock/boundary-layer interactions. *Physical review fluids*, 3, 2018.

[3] Mirko Zaccara, Joshua Edelman, and Gennaro Cardone. A general procedure for infrared thermography heat transfer measurements in hypersonic wind tunnels. *International Journal of Heat and Mass Transfer*, 163, 2020.

[4] Gennaro Cardone. Ir heat transfer measurements in hypersonic plasma flows. *Quantitative InfraRed Thermography Journal*, 4:233–251, 2007.

[5] Hajime Nakamura. Spatio-temporal measurement of convective heat transfer using infrared thermography. Heat Transfer - Theoretical Analysis, Experimental Investigations and Industrial Systems, pages 545–572. InTech, 2011.

[6] Irina Znamenskaya. Methods for panoramic visualization and digital analysis of thermophysical flow fields. *Scientific visualization*, 13(3):125–158, 2021.

[7] Vladimir Vavilov. Infrared thermography and thermal control. pages 45–544. ID Spectrum, 2009.

[8] Giovanni Carlomagno and Gennaro Cardone. Infrared thermography for convective heat transfer measurements. *Experiments in Fluids*, 49(6):1187–1218, 2010.

[9] I. Kudryashov, Alexander Lutsky, and Yana Khankhasaeva. Numerical simulation of the influence of energy deposition on the base flow. *Mathematical Models and Computer Simulations*, 8, 2014.

[10] Hermann Schlichting. Grenzschichttheorie. Braun Verlag, Karlsruhe, 1965.